Monthly Notices
of the
ROYAL ASTRONOMICAL SOCIETY

MNRAS **479,** 517–535 (2018)
Advance Access publication 2018 May 31

doi:10.1093/mnras/sty1420

Swift UVOT grism observations of nearby Type Ia supernovae – I. Observations and data reduction

Y.-C. Pan,[1]★ R. J. Foley,[1] A. V. Filippenko[2,3]† and N. P. M. Kuin[4]

[1]*Department of Astronomy and Astrophysics, University of California, Santa Cruz, CA 95064, USA*
[2]*Department of Astronomy, University of California, Berkeley, CA 94720-3411, USA*
[3]*Miller Institute for Basic Research in Science, University of California, Berkeley, CA 94720, USA*
[4]*Mullard Space Science Laboratory/University College London, Holmbury St Mary, Dorking, Surrey RH5 6NT, UK*

Accepted 2018 May 25. Received 2018 May 24; in original form 2018 February 27

ABSTRACT

Ultraviolet (UV) observations of Type Ia supernovae (SNe Ia) are useful tools for understanding progenitor systems and explosion physics. In particular, UV spectra of SNe Ia, which probe the outermost layers, are strongly affected by the progenitor metallicity. In this work, we present 120 *Neil Gehrels Swift Observatory* UV spectra of 39 nearby SNe Ia. This sample is the largest UV ($\lambda < 2900$ Å) spectroscopic sample of SNe Ia to date, doubling the number of UV spectra and tripling the number of SNe with UV spectra. The sample spans nearly the full range of SN Ia light-curve shapes ($\Delta m_{15}(B) \approx 0.6$–$1.8$ mag). The fast turnaround of *Swift* allows us to obtain UV spectra at very early times, with 13 out of 39 SNe having their first spectra observed $\gtrsim$1 week before peak brightness and the earliest epoch being 16.5 d before peak brightness. The slitless design of the *Swift* UV grism complicates the data reduction, which requires separating SN light from underlying host-galaxy light and occasional overlapping stellar light. We present a new data-reduction procedure to mitigate these issues, producing spectra that are significantly improved over those of standard methods. For a subset of the spectra we have nearly simultaneous *Hubble Space Telescope* UV spectra; the *Swift* spectra are consistent with these comparison data.

Key words: supernovae: general.

1 INTRODUCTION

Type Ia supernovae (SNe Ia) are luminous distance indicators that were used to first discover the accelerating expansion of the Universe (Riess et al. 1998; Perlmutter et al. 1999). SNe Ia provide a direct route to probe the nature of the dark energy that drives the accelerated expansion. While SNe Ia are not perfect standard candles, they can be standardized via the tight relation between SN Ia light-curve width and luminosity (width–luminosity relation, WLR; Phillips 1993) and between SN Ia optical colour and luminosity (Riess, Press & Kirshner 1996)—more luminous SNe Ia are bluer and have broader, slower evolving light curves. After making these corrections, we are able to use these *standardizable* candles for cosmological inferences.

Observational evidence indicates that an SN Ia is the result of the thermonuclear explosion of an accreting carbon–oxygen white dwarf (WD) star in a close binary system (e.g. Hillebrandt & Niemeyer 2000; Hillebrandt et al. 2013; Maoz, Mannucci & Nelemans 2014). Theoretically, the amount of ^{56}Ni synthesized during the thermonuclear explosion affects the optical opacity and changes the 'width' of an SN light curve, with slower declining SNe Ia having more opacity and higher luminosities (Hoeflich et al. 1996). Making empirical corrections based on light-curve width and colour, SNe Ia become exquisite distance indicators with a distance scatter below 8 per cent (e.g. Conley et al. 2008; Wang et al. 2009b; Kelly et al. 2015). However, that remaining distance scatter is *intrinsic scatter*, beyond any measurement error, and must be related to physics unaccounted for in the standardization.

Current SN cosmology analyses assume that SNe Ia across all redshifts have the same peak luminosity after standardizing by the WLR. However, new observations showed that even after standardization, luminosity still correlates with the large-scale host-galaxy environment (e.g. Kelly et al. 2010; Lampeitl et al. 2010; Sullivan et al. 2010; Pan et al. 2014). SNe Ia in galaxies of higher metallicities have (on average) higher corrected luminosities than those with lower metallicities. SNe Ia with identical progenitors except for metallicity are predicted to produce different amounts of ^{56}Ni. Higher progenitor metallicity will result in a larger fraction of stable iron-group elements (IGEs) and less ^{56}Ni in the SN explosion, and therefore fainter peak luminosity (Timmes, Brown & Truran 2003).

★ E-mail: ypan6@ucsc.edu
† Miller Senior Fellow.

Table 1. Summary of *Swift* UVOT grism observations of the SN Ia sample in this work.

SN name	Host	Redshift	$\Delta m_{15}(B)^a$ (mag)	UT obs. date	$T_{\rm exp}$ (s)	$T_{\rm exp}$ used^b (s)	Phase (d)	LC Ref.^{c}
SN 2005am	NGC 2811	0.0079	1.45(03)	2005-03-08.02	2781.73	1097.31	0.0	Brown et al. (2005)
SN 2005cf	MCG-01-39-03	0.0065	1.05(03)	2005-06-04.71	1897.12	1897.12	− 7.9	Wang et al. (2009a)
				2005-06-05.71	1958.95	1958.95	− 6.9	
				2005-06-06.72	1572.61	1572.61	− 5.9	
				2005-06-08.80	1726.76	1726.76	− 3.8	
				2005-06-09.52	626.97	626.97	− 3.1	
				2005-06-10.74	713.38	713.38	− 1.9	
				2005-06-11.61	2022.68	2022.68	− 1.0	
				2005-06-16.36	1812.21	1812.21	3.7	
				2005-06-17.30	1670.84	1670.84	4.6	
				2005-06-20.71	2002.30	2002.30	8.0	
				2005-06-26.34	2004.37	2004.37	13.6	
				2005-06-29.11	2122.21	2122.21	16.3	
SN 2005df	NGC 1559	0.0044	1.12(00)	2005-08-11.06	1634.74	1634.74	− 6.1	Krisciunas et al. (2017)
				2005-08-14.13	983.46	983.46	− 3.1	
				2005-08-17.94	2018.12	2018.12	0.7	
				2005-08-21.57	422.10	422.10	4.4	
SN 2005ke	NGC 1371	0.0049	1.76(01)	2005-11-20.44	1952.35	318.56	− 4.7	Folatelli et al. (2010)
				2005-11-22.42	3657.86	3657.86	− 2.7	
SN 2006dd	NGC 1316	0.0059	1.08(01)	2006-07-14.51	3956.35	3956.35	11.0	Stritzinger et al. (2010)
SN 2007sr	NGC 4038	0.0055	0.92(04)	2007-12-20.69	1992.51	1992.51	6.7	Folatelli et al. (2013)
				2007-12-25.12	3729.30	3729.30	11.1	
				2007-12-26.15	3391.09	3391.09	12.1	
				2007-12-28.06	5988.71	5988.71	14.0	
SN 2008Q	NGC 524	0.0079	1.41(05)	2008-02-09.23	5755.24	4916.04	− 0.2	Childress et al. (2015)
				2008-02-09.79	5097.28	3192.17	4.3	
SN 2008hv	NGC 2765	0.0136	1.25(01)	2008-12-11.66	8522.28	8522.28	− 5.1	Folatelli et al. (2013)
				2008-12-14.74	8584.80	8584.80	− 2.0	
SN 2009Y	NGC 5728	0.0093	1.21(00)	2009-02-07.64	7602.16	1352.78	− 6.2	Friedman et al. (2015)
				2009-02-08.41	8627.93	5933.63	− 5.5	
				2009-02-10.56	13 392.66	10 862.94	− 3.3	
				2009-02-11.86	6269.84	6269.84	− 2.0	
				2009-02-13.16	18 123.06	14 394.74	− 0.7	
				2009-02-18.49	13 208.81	11 059.49	4.6	
SN 2009an	NGC 4332	0.0092	1.44(00)	2009-03-03.63	14 473.74	12 650.73	− 4.5	Friedman et al. (2015)
				2009-03-04.17	4265.17	4265.17	− 4.0	
				2009-03-10.96	8431.56	1624.79	2.7	
				2009-03-12.24	10 282.27	8659.64	4.0	
SN 2009dc	UGC 10064	0.0214	0.72(03)	2009-04-30.85	3707.84	3283.08	5.3	Silverman et al. (2011)
				2009-05-01.22	5110.87	3978.95	5.8	
SN 2009ig	NGC 1015	0.0088	0.89(00)	2009-08-24.12	7023.63	5943.86	− 12.8	Foley et al. (2012a)
				2009-08-24.76	5516.39	5516.39	− 12.1	
				2009-08-25.69	4547.29	3031.54	− 11.2	
				2009-08-27.57	14 024.93	12 737.63	− 9.3	
				2009-09-01.34	5857.20	1624.77	− 4.6	
				2009-09-03.70	13 531.05	13 531.05	− 2.3	
				2009-09-07.34	18 060.624	18 060.62	1.3	
				2009-09-14.26	18 009.77	16 657.00	8.2	
SN 2010ev	NGC 3244	0.0092	1.12(02)	2010-07-12.13	17 820.81	6325.86	5.0	Gutiérrez et al.(2016)
SN 2011B	NGC 2655	0.0047	1.38(16)	2011-01-15.20	10263.21	9654.62	− 6.0	Brown et al. (2017)
SN 2011aa	UGC 3906	0.0124	0.59(07)	2011-02-28.15	7519.65	6271.86	8.1	Brown et al. (2014)
SN 2011ao	IC 2973	0.0107	1.00(00)	2011-03-08.69	10 654.46	10 654.46	− 9.5	Friedman et al. (2015)
				2011-03-09.48	6633.80	6633.80	− 8.7	
				2011-03-15.74	7878.21	7878.21	− 2.5	
				2011-03-16.27	1694.51	1694.51	− 2.0	
SN 2011by	NGC 3972	0.0028	1.14(03)	2011-05-01.58	9456.18	9456.18	− 8.3	Silverman, Ganeshalingam & Filippenko (2013)
				2011-05-04.01	37.16	37.16	− 5.9	
				2011-05-05.50	7788.52	7144.74	− 4.4	
				2011-05-07.26	9237.24	9237.24	− 2.6	
				2011-05-10.54	9560.79	9560.79	0.6	
SN 2011fe	NGC 5457	0.0008	1.11(00)	2011-08-28.52	9437.18	9437.18	− 13.8	Munari et al. (2013)

Table 1 – *continued*

SN name	Host	Redshift	$\Delta m_{15}(B)^a$ (mag)	UT obs. date	T_{exp} (s)	T_{exp} used[b] (s)	Phase (d)	LC Ref.[c]
				2011-09-03.63	8591.08	8591.08	– 7.7	
				2011-09-07.28	7218.58	5878.83	– 4.0	
				2011-09-10.65	7679.62	7679.62	0.6	
				2011-09-13.56	6156.47	6156.47	2.3	
				2011-09-16.24	6127.14	5195.36	5.0	
				2011-09-26.19	5507.78	5507.78	14.9	
				2011-09-29.26	3838.31	3838.31	18.0	
				2011-10-08.32	2596.54	2596.54	27.0	
				2011-10-11.73	6490.82	6490.82	30.4	
SN 2011iv	NGC 1404	0.0065	1.69(05)	2011-12-05.26	8015.13	3048.35	– 5.7	Foley et al. (2012b)
				2011-12-06.85	2858.51	2858.51	– 4.1	
				2011-12-07.48	5627.53	5387.54	– 3.5	
				2011-12-09.83	644.11	622.89	– 1.2	
				2011-12-11.56	11 926.23	11 926.23	0.5	
SN 2012cg	NGC 4424	0.0014	1.04(00)	2012-05-23.38	17 685.15	15 126.62	– 12.6	Munari et al. (2013)
				2012-05-26.86	16 944.41	12 267.43	– 9.1	
SN 2012dn	ESO 462-G016	0.0101	1.08(03)	2012-07-23.28	3811.96	1188.78	– 1.5	Brown et al. (2014)
SN 2012fr	NGC 1365	0.0055	0.85(05)	2012-11-03.34	5927.61	5927.61	– 9.1	Zhang et al. (2014)
				2012-11-04.67	11 276.43	11 276.43	– 7.8	
				2012-11-07.67	12 656.91	12 656.91	– 4.8	
				2012-11-08.14	3512.32	3512.32	– 4.3	
				2012-11-11.62	4547.31	4547.31	– 0.9	
				2012-11-13.39	16 431.98	15 312.46	0.9	
SN 2012ht	NGC 3447	0.0036	1.39(05)	2012-12-26.35	13 501.33	13 501.33	– 8.3	Yamanaka et al. (2014)
				2012-12-28.32	6860.62	6860.62	– 6.3	
				2012-12-31.46	5590.03	4057.27	– 3.1	
SN 2013aa	NGC 5643	0.0040	0.80(03)	2013-02-19.73	5625.08	5625.08	– 1.3	Maguire et al. (2013)
				2013-02-26.74	5807.38	1503.57	5.7	
SN 2013cg	NGC 2891	0.0080	–	2013-05-12.95	11 846.95	11 846.95	0.0	Spectrum[d]
SN 2014J	NGC 3034	0.0007	0.95(01)	2014-01-25.67	11 245.94	8649.39	– 6.3	Foley et al. (2014)
				2014-02-01.37	9043.35	7999.93	0.4	
				2014-02-03.08	9347.16	9347.16	2.1	
				2014-02-04.88	4401.08	4401.08	3.9	
				2014-02-05.87	4807.05	3639.29	4.9	
				2014-02-07.61	4175.04	3402.30	6.6	
				2014-02-08.77	4099.32	3239.30	7.8	
iPTF14bdn	UGC 8503	0.0156	0.84(05)	2014-06-08.70	7272.02	7272.02	– 5.7	Smitka et al. (2015)
				2014-06-11.52	4589.50	4589.50	– 2.9	
				2014-06-19.60	9142.26	9142.26	5.0	
				2014-06-23.25	8621.41	8621.41	8.6	
				2014-07-02.32	5659.88	5659.88	17.5	
ASASSN-14lp	NGC 4666	0.0051	0.80(05)	2014-12-13.54	16 848.62	16 848.62	– 11.2	Shappee et al. (2016)
				2014-12-18.47	17 369.47	10 806.60	– 6.3	
SN 2016ccz	MRK 685	0.0150	1.00(02)	2016-05-28.87	11 505.85	11 505.85	– 1.2	Foley et al. (2018)
SN 2016coj	NGC 4125	0.0045	1.33(03)	2016-06-07.02	12 877.91	7549.49	– 2.1	Foley et al. (2018)
SN 2016eiy	ESO 509-IG064	0.0087	–	2016-08-05.58	6697.64	4556.10	0.6	Spectrum[e]
				2016-08-10.77	4031.31	4031.31	5.7	
SN 2016ekg	PGC 67803	0.0171	–	2016-08-06.31	7185.58	6105.81	– 0.7	Spectrum[f]
				2016-08-09.56	5138.10	5138.10	2.5	
SN 2016eoa	NGC 0083	0.0208	1.35(03)	2016-08-17.51	13 133.66	13 133.66	1.8	Foley et al. (2017)
SN 2016fff	UGCA 430	0.0114	1.49(05)	2016-08-28.87	6315.70	5408.91	2.4	Swope[g]
SN 2016gsb	ESO 555-G029	0.0097	–	2016-10-04.44	11 189.93	7405.62	– 2.5	Spectrum[h]
SN 2016itd	UGC 9165	0.0175	–	2016-12-13.42	11 628.96	11 628.96	5.3	Spectrum[i]
SN 2017cbv	NGC 5643	0.0040	1.06(00)	2017-03-12.53	11 914.14	5005.92	– 16.5	Hosseinzadeh et al. (2017)
				2017-03-17.58	11 081.64	92 39.51	– 11.5	
				2017-03-24.48	12 373.66	12 373.66	– 4.6	
SN 2017erp	NGC 5861	0.0062	–	2017-06-17.35	8495.45	4743.82	– 7.1	Swope[g]

Table 1 – *continued*

SN name	Host	Redshift	$\Delta m_{15}(B)^a$ (mag)	UT obs. date	T_{exp} (s)	T_{exp} used[b] (s)	Phase (d)	LC Ref.[c]
				2017-06-19.18	10 173.46	8581.91	− 5.3	
SN 2018aoz	NGC 3923	0.0058	–	2018-04-12.82	2323.53	2323.53	− 2.2	Spectrum[j]

[a]The *B*-band decline 15 d after the peak brightness.
[b]The total exposure time of the exposures actually used for data reduction and SNR calculation in this work.
[c]The reference of SN photometric properties adopted in this work.
[d]The epoch of peak brightness is estimated from the optical spectrum observed on 2013 May 26 UT under the ANU WiFeS SuperNovA Programme (AWSNAP; Childress et al. 2016).
[e]The epoch of peak brightness is estimated from the optical spectrum observed on 2016 July 26 UT under the Public ESO Spectroscopic Survey for Transient Objects (PESSTO; Smartt et al. 2015) program.
[f]The epoch of peak brightness is estimated from the optical spectrum observed on 2016 August 1 UT under the PESSTO program.
[g]Using the light curves obtained from Swope telescope at Cerro Las Campanas.
[h]The epoch of peak brightness is estimated from the optical spectrum observed on 2016 October 1 UT under the PESSTO program.
[i]The epoch of peak brightness is estimated from the optical spectrum observed on 2016 December 6 UT by KANATA 1.5-m telescope.
[j]The epoch of peak brightness is estimated from the optical spectrum observed on 2018 April 2 UT by FLOYDS-S telescope.

Table 2. Summary of *Swift* UVOT grism observations of the SNe Ia NOT included in this work owing to either extremely low SNR or serious background contamination in the UV.

SN name	UT obs. date	*Swift* obs. ID
SN 2005am	2005-03-09	30010007
	2005-03-18	30010036
	2005-03-22	30010051
	2005-03-24	30010057
SN 2005hk	2005-11-08	30338004
SN 2007sr	2007-12-21	31073004
	2007-12-22	31073007
	2007-12-23	31073010
	2007-12-24	31073013
SN 2010ev	2010-07-05	31751001
SN 2014J	2014-01-23	33124001
SN 2016gfr	2016-09-21	34732002
OGLE16dha	2016-09-30	34742002
	2016-10-05	34742004
SN 2018gv	2018-01-23	10521003
	2018-01-23	10521005
SN 2018xx	2013-02-23	10572004

Theoretical studies indicate that the higher progenitor metallicity will increase the IGEs in the outer layers of the SN, which will cause greater UV line blanketing (Lentz et al. 2000). Consequently, the progenitor metallicity will not change the optical spectral energy distribution (SED) of an SN Ia significantly, but will dramatically change its UV SED. This effect is also seen in recent observations of the 'twin' SN 2011 by and SN 2011fe (Foley & Kirshner 2013). The two SNe have nearly identical optical light-curve widths and spectra but very different UV spectra. Thus, the WLR is insufficient to calibrate the luminosity, resulting in increased Hubble-diagram scatter. The UV SED is essential to detect this metallicity effect.

The earliest UV observations of SNe date back to early 1980s, with a handful of SNe Ia observed by the *International Ultraviolet Explorer* satellite (e.g. Cappellaro, Turatto & Fernley 1995). The launch of the *Hubble Space Telescope* (*HST*) marked a milestone in obtaining high-quality UV spectra to study the progenitor composition and explosion mechanisms of SNe Ia (e.g. Maguire et al. 2012; Pan et al. 2015; Foley et al. 2016). However, the current *HST* sample is too small (e.g. 9 SNe in Foley et al. 2016) to cover all of the parameter space, such as light-curve width, ejecta velocity, and progenitor metallicity. Thus, we try to increase the sample of SNe Ia with UV spectra obtained with the *Neil Gehrels Swift Observatory* (Gehrels et al. 2004).

A good amount of *Swift* UV spectroscopy has been published by recent studies (e.g. Bufano et al. 2009; Foley et al. 2012a; Brown et al. 2014; Smitka et al. 2016; Gall et al. 2017). Although *HST* has superior UV capabilities compared to *Swift*, the fast turnaround of *Swift* and its efficiency to obtain the data are unmatched. The earliest UV spectrum of an SN Ia published before this work was obtained from *Swift* (SN 2009ig; Foley et al. 2012a); it was observed ∼13 d before the peak brightness. Extremely early observations with *Swift* are complementary to the existing *HST* UV sample.

However, the slitless design of the *Swift* observations makes the spectrum more likely to be contaminated by nearby background sources. This not only complicates the data reduction, but also makes the interpretation of *Swift* data sets difficult. Traditional methods using *Swift*/Ultraviolet–Optical Telescope (UVOT; Roming et al. 2004) grism data-reduction software (UVOTPY; Kuin 2014) have been widely used, but they become less reliable when reducing spectra that are seriously contaminated by nearby background sources. A more effective decontamination technique has been developed by Smitka et al. (2016). However, their method requires a template observation of the galaxy with the same spacecraft roll angle at late times (usually >1 yr after SN explosion), which weakens the advantage of *Swift* (i.e. its fast turnaround). A relatively fast and correct reduction of early-time data is useful for assessing and scheduling the follow-up observations of young transients.

In this work, we present an SN sample that is more than three times larger than that of the *HST* UV sample. We improve the *Swift* UVOT grism data-reduction procedure to better extract SN spectra. This allows us to produce more accurate *Swift* spectra, which we will exploit in future analyses.

A plan of the paper is as follows: In Section 2 we introduce the selection and observations of our SN Ia sample. Section 3 discusses the data-reduction techniques. We present the spectra in

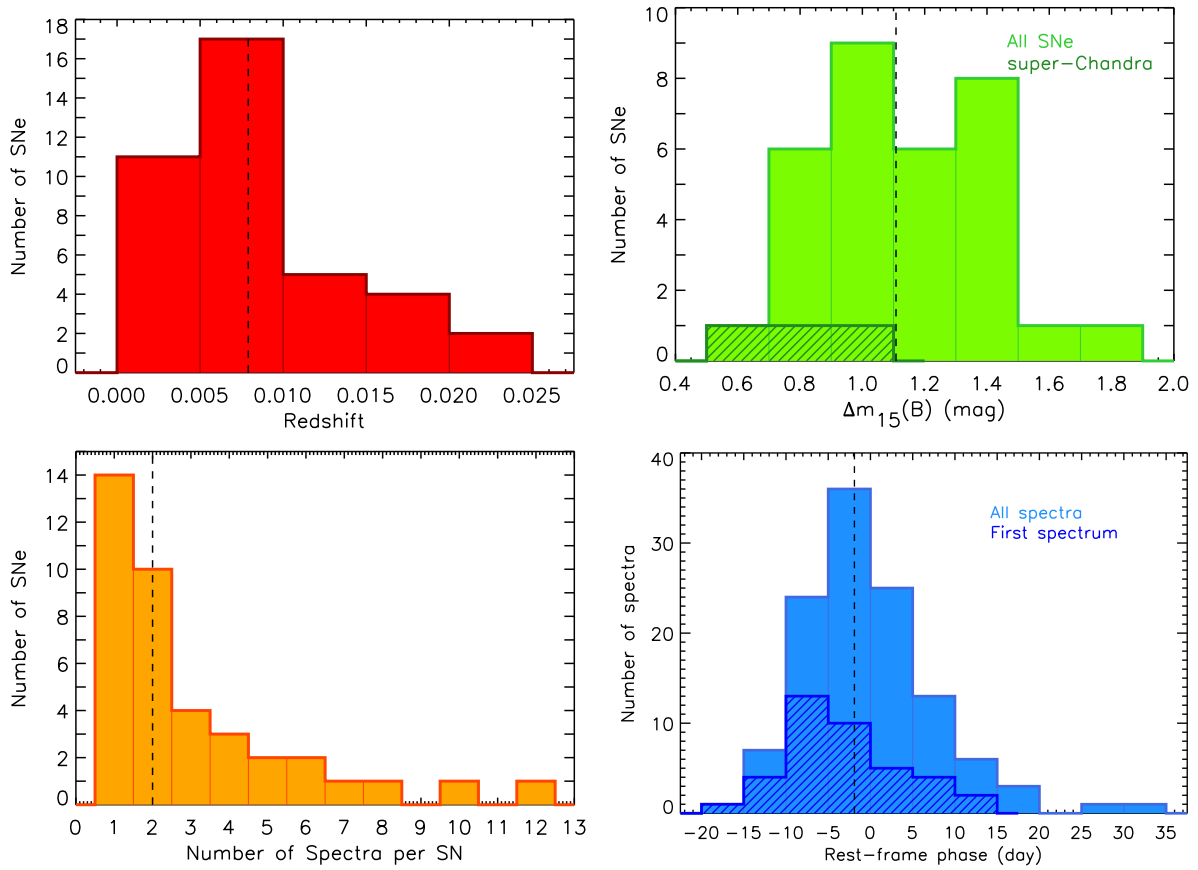

Figure 1. Redshift (upper left), $\Delta m_{15}(B)$ (upper right), number of spectra per SN (lower left), and rest-frame phase (lower right) distributions of the *Swift* UV SN Ia sample presented in this work. $\Delta m_{15}(B)$ represents the *B*-band decline 15 d after peak *B*-band brightness. In the upper-right panel, we separate our sample into those classified as normal SNe Ia (solid histogram) and 'super-Chandrasekhar' SNe Ia (dashed histogram). In the lower-right panel, we also overplot the phase distribution of the first spectrum (dashed histogram). The vertical dashed line in each panel shows the median of the distribution.

Section 4 and summarize our results in Section 5. Throughout this paper, we assume $H_0 = 70\ \mathrm{km\,s^{-1}\,Mpc^{-1}}$ and a flat universe with $\Omega_M = 0.3$.

2 OBSERVATIONS

2.1 SN sample selection

Most of the SNe in our sample were observed as part of our dedicated Guest Investigator programs (GI–04047, GI–5080130, PI Filippenko; GI–6090689, GI–8110089, GI–1013136, GI–1215205, PI Foley). However, the full sample contains all SNe Ia observed with the UVOT/UV grism by *Swift* (excluding spectra that are not useful for further analysis; see below for more details).

The UVOT has a relatively small aperture (30 cm), and so only relatively nearby SNe Ia are sufficiently bright (distance modulus $\mu \lesssim 35$ mag, corresponding to $V_{\rm max} \lesssim 15$ mag) to produce high-quality spectra in reasonable exposure times. We desired spectra of the SNe before or near peak brightness, and therefore most SNe in the sample were discovered 1–2 weeks before peak brightness.

The sample presented here contains 120 *Swift*/UVOT Grism spectra of 39 SNe Ia, with 20 SNe observed through our *Swift* programs and another 19 SNe selected from the *Swift* data archive that have UV spectra. The complete list of SNe in this work can be found in Table 1. Besides these 120 spectra, there are 17 observations from which we cannot extract any useful data or that were highly contaminated by background sources. We summarize them in Table 2.

In Fig. 1, we present the redshift, $\Delta m_{15}(B)$ (the *B* band declines 15 d after peak brightness), number of spectra per SN, and rest-frame phase distributions of our sample. The median redshift of the sample is 0.0079, with the closest object having $z = 0.0006$ ($D = 3.3$ Mpc; SN 2014J) and the most distant SN having $z = 0.0214$ ($D = 93$ Mpc; SN 2009dc). The $\Delta m_{15}(B)$ of our sample ranges from 0.6 to 1.8 mag (median of 1.1 mag), with three objects classified as super-*Chandra* SNe Ia having $\Delta m_{15}(B) = 0.72$ (SN 2009dc), 0.59 (SN 2011aa), and 1.08 mag (SN 2012dn). We lack sufficient data to measure $\Delta m_{15}(B)$ of 7 SNe.

A large fraction of the SNe in our sample (24 out of 39) have multiple epochs of UV spectra, with a median of two spectra per SN. This makes our sample particularly useful in studying UV spectral evolution. The SN phase is relative to the epoch of peak optical brightness. For the six SNe where we do not have light curves, the epoch of peak brightness is estimated by fitting the optical spectra with SNID (Blondin & Tonry 2007). The median phase (in the rest frame) of the first observation of an SN and all spectra is −4.5 and −1.9 d, respectively. Among the 39 SNe, 13

have spectra $\gtrsim$1 week before peak brightness, 29 have pre-peak spectra, and 34 have spectra before 5 d after peak brightness. The earliest spectrum in our sample (of SN 2017cbv) was observed 16.5 d before peak brightness. It was observed by *Swift* <2 d after explosion. This shows the fast turnaround of *Swift* and its ability to obtain a spectrum at extremely early times.

2.2 *Swift* observations

The spectroscopic observations were performed by the *Swift* UVOT (Roming et al. 2004). The UVOT provides UV and optical spectroscopy with either slitless UV-grism or *V*-grism. In this work, we focus on the UV-grism observations, with a wavelength coverage of ~1700–5000 Å and the UV response optimized in the 2000–3400 Å region.

Owing to the slitless design of the UVOT for spectroscopy, the data image contains both zeroth-order and higher order emission (see Fig. 2 for an example). We asked our targets to be observed under the 'clocked mode' when possible. Observing in clocked mode reduces the contamination from zeroth-order images of field stars (e.g. those marked in the lower panel of Fig. 2) where the first-order light falls on the detector – and comes close to a slit spectrograph in the occulted region.

Given the brightness of our targets, we requested an average exposure time $T_{\rm exp} = 15$ ks in our own programs to obtain a good UV spectrum near peak brightness; however, such long exposures were rarely obtained because of various observing constraints. The exposure times ranged from 0.6 to 18 ks with a median of 8.5 ks.

3 DATA REDUCTION

Compared to typical slit spectroscopy, the slitless design of the *Swift* UVOT grism makes the target spectrum more likely to be contaminated by nearby background sources. Although 'clocked mode' is adopted for most of our observations, higher order spectra (e.g. from either the host galaxy or field stars) could still overlay or fall close to our targets, affecting the background subtraction.

The other major complication for slitless spectra is that the entire galaxy along the dispersion direction, instead of the region directly coincident with the SN, will contaminate the spectrum. These regions are spatially offset from the SN and other regions of the galaxy, and therefore light from nearby wavelengths can contaminate the SN spectrum (effectively 'smearing' the galaxy spectrum in the wavelength direction).

Smitka et al. (2016) attempted to address these problems by observing a template image of the galaxy long after the SN faded in nearly the same configuration (e.g. clocking, pointing, and roll angle) as the original data image. They measure the background at the same location in the template image and then subtracted that from the target spectrum. This decontamination technique is effective in reducing any contamination in the SN spectrum. However, the template image can only be obtained after the SN has faded away (usually $\gtrsim$1 yr after peak brightness). Given the fast turnaround of *Swift*, it would be ideal to be able to perform an effective data reduction on a shorter timescale. Moreover, the exposure time for the template spectrum must be long (i.e. comparable to that of the data image), so as to not adversely affect the SNR of the final host-subtracted SN spectrum.

We developed our own pipeline to reduce UVOT grism data, building upon the *Swift* UVOTPY software (Kuin 2014; Kuin et al. 2015). We follow the standard procedures in UVOTPY, such as target extraction, background subtraction, wavelength calibration, and flux

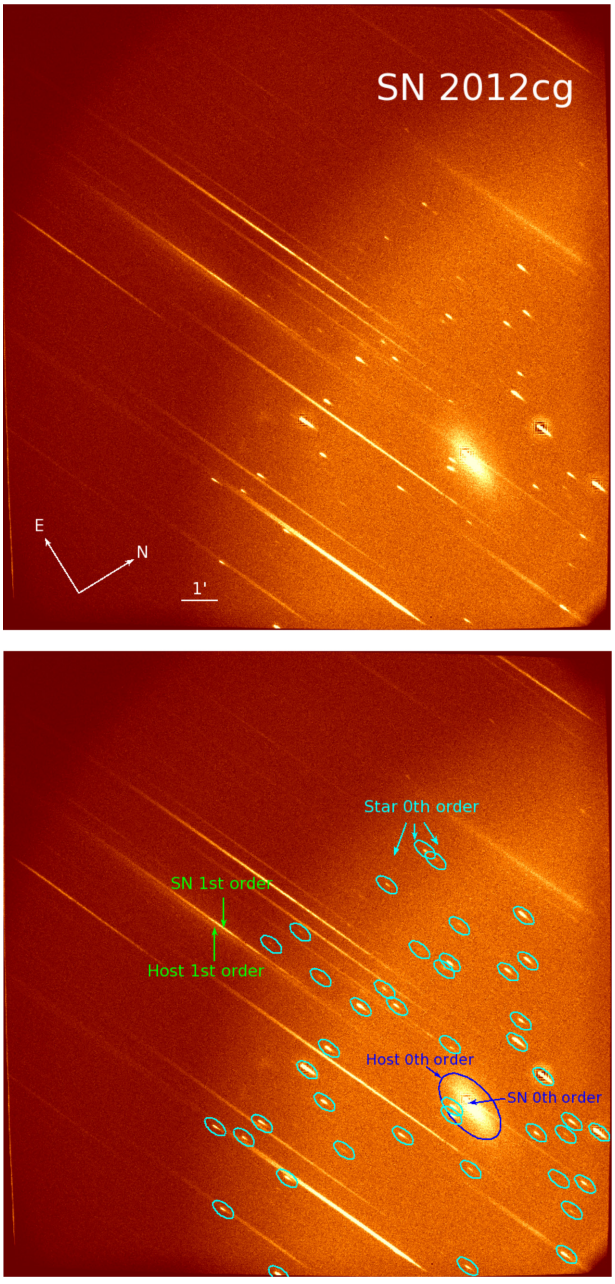

Figure 2. *Upper panel*: *Swift* data image of SN 2012cg. *Lower panel*: Same as upper panel, but with annotations. The first-order spectra from the SN and its host galaxy are marked with green arrows. The zeroth-order light from the SN and its host galaxy are marked with blue arrows. All zeroth-order images from nearby bright stars are marked in cyan. The image is 17 arcmin × 17 arcmin.

calibration. However, our pipeline measures the background in a different way. Instead of creating a smoothed background image by averaging the regions above and below the target spectrum, we extract background spectra above and below the target with customizable offsets and sizes and then subtract the interpolated (at the position of the target) background spectrum.

We illustrate the target and background extractions in Fig. 3. The top panel shows the first-order spectrum of SN 2012cg from Fig. 2. The contamination from the host galaxy spectrum is clearly seen above the SN trace. The aperture used to extract the SN spectrum is

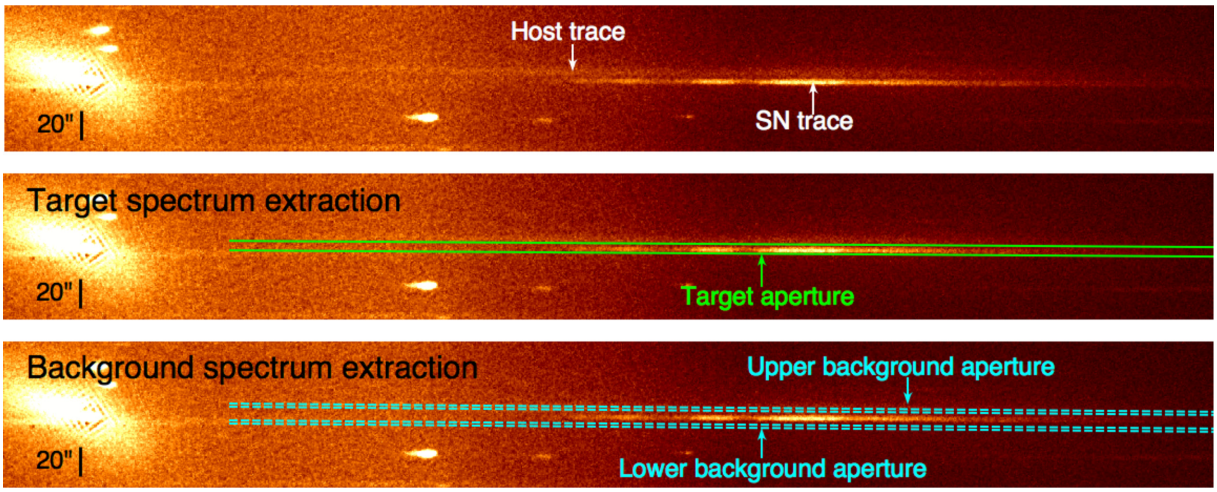

Figure 3. Rotated and expanded version of the SN 2012cg image shown in Fig. 2. The top, middle, and bottom panels mark the SN and host-galaxy spectra, the SN extraction aperture, and the background regions, respectively.

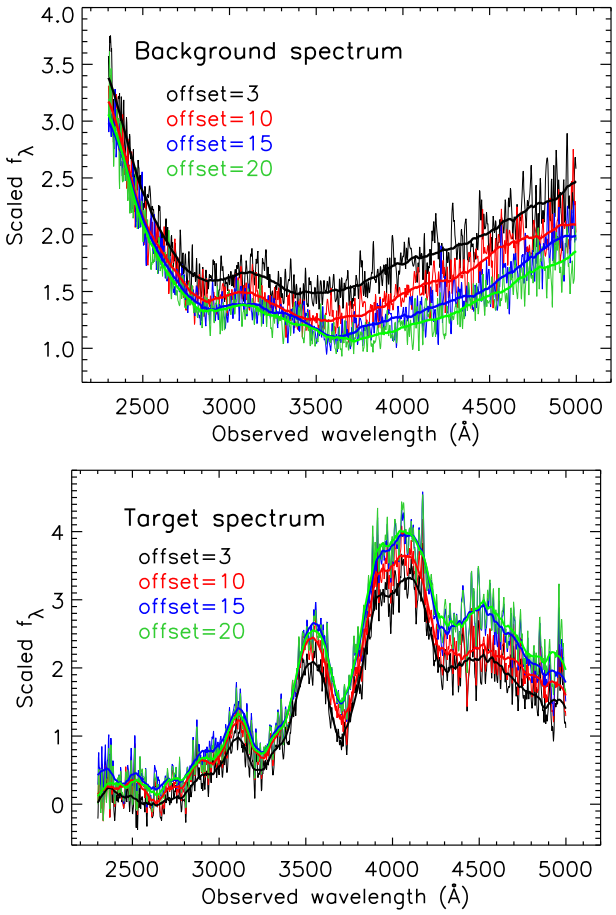

Figure 4. *Upper panel*: Comparison of interpolated background spectra by varying the offset (in pixels) of the background channel relative to the SN aperture as shown in Fig. 3. Here the background spectra with offsets of 3 (the value ultimately chosen for this spectrum), 10, 15, 20 pixels are shown as black, red, blue, and green curves, respectively. *Bottom panel*: The resulting SN spectra for the background offsets shown in the upper panel plotted in their corresponding colours. Savitzky–Golay smoothed spectra are overplotted, as thick lines, in both panels.

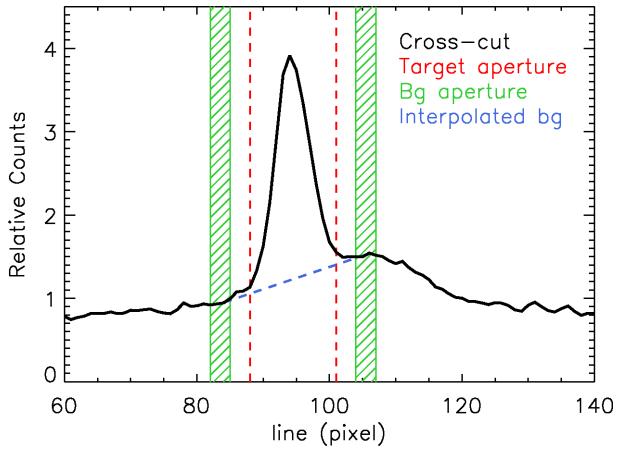

Figure 5. Spatial profile of the SN and background perpendicular to the SN trace (a 'cross-cut') for the data presented in Fig. 3 (black curve). The red dashed lines define the aperture used to extract the SN spectrum. The regions used to define the background are marked by hashed green regions. The interpolated background used for final background subtraction is shown as a blue dashed line. In this example, the size of the target aperture is set to 13 pixels (1.8σ). The size of each background region is 3 pixels. The upper and lower background regions are offset by 3 pixels from the edge of the target aperture.

marked in the panel. For bright objects, we generally adopt an aperture size similar to that of the UVOTPY default (i.e. 2.5σ). Here the aperture size is controlled by σ, the standard deviation of a Gaussian distribution used to fit the count rate of the cross-dispersion profile of the spectrum (for details, see Kuin et al. 2015). Smaller apertures are recommended for fainter sources or those with nearby contamination. For SN 2012cg, as displayed in Fig. 3, we use an aperture size of 1.8σ. When using smaller apertures, we rescale the flux to match that of the default aperture size which was used for flux calibration and coincidence-loss correction.

We demonstrate the background extraction in the bottom panel of Fig. 4. The two apertures used to extract the background spectra above and below the target are shown in the panel. They are offset from the target along the dispersion axis to trace the curvature of the spectrum. The background spectrum can be sensitive to the offset

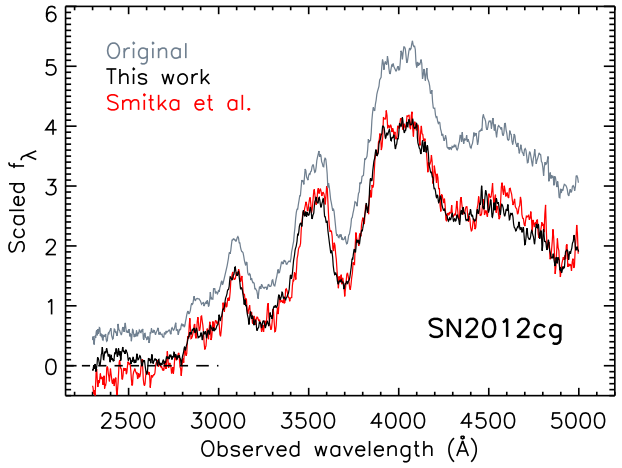

Figure 6. Comparison of our fully reduced spectrum of SN 2012cg (in black) to reduced spectra produced by the original data-reduction pipeline (in grey) and by the Smitka et al. (2016) decontamination technique (in red). The dashed line marks the level of zero flux.

of the apertures from the target. Because of the contamination from the underlying host-galaxy spectrum, the flux of the background spectrum can vary by a factor of ∼2 depending on different offsets, altering the final target spectrum significantly; this effect is shown in Fig. 4. To accurately estimate the local background, we generally extract the background spectrum as close to the SN as possible, selecting an aperture size that does not overlap with the SN aperture. This is achieved by inspecting the 'cross-cut' of the spectrum (i.e. the spatial flux distribution perpendicular to the trace; see Fig. 5). For SN 2012cg, we offset the background apertures from the edge of the target aperture by 3 pixels to not only remove the host-galaxy light, but also not to include the SN light. Larger offsets result in incorrect background subtraction and increase the contamination from the host galaxy.

After the target extraction and background subtraction, we wavelength- and flux-calibrate each spectrum following the procedures in UVOTPY. Given the large uncertainty in wavelength calibration (the accuracy is ∼9 Å for the UV grism clocked mode; Kuin et al. 2015), we shift the zeropoint of the wavelength solution for each individual exposure by cross-correlating the spectrum to that of another spectrum (either an *HST* or a ground-based spectrum) at a similar phase.

Each epoch of spectroscopy usually consists of several short exposures, with each observed under slightly different conditions that slightly change the flux and wavelength of the spectrum. Therefore, we repeat the same reduction procedure with each individual exposure before combining all spectra into a single spectrum. If no comparison spectrum is available, we simply shift the wavelength of all the exposures to match the mean value. The shift of our *Swift* spectra ranges from ∼−30 to +30 Å, with an average of −6 Å relative to the *HST* spectra.

For bright zeroth-order contamination (e.g. field stars) falling close to the target spectrum, our pipeline can identify those sources (through the background spectrum) more easily than the old method, but it is generally inferior to reductions using a template spectrum (i.e. Smitka et al. 2016). We cross-check bright sources ($B < 18$ mag) from the USNO-B1.0 catalogue (Monet et al. 2003) and remove the affected pixels when producing the final spectrum.

4 RESULTS

4.1 Comparison of data-reduction methods

Fig. 6 shows a comparison of spectra reduced using the method described in Section 3 to the same spectra reduced using the default UVOTPY software and the Smitka et al. (2016) decontamination method. The spectrum produced through our method agrees well with that from Smitka et al. (2016). However, the spectrum reduced by the default pipeline is clearly offset in flux from the other two spectra. This is likely caused by incorrect host-galaxy subtraction (see Figs 3 and 4). The default UVOTPY method underestimates the underlying background, resulting in a spectrum with higher flux at all wavelengths (i.e. with additional light from the host galaxy). Our new method removes the host contamination and performs the background subtraction more correctly.

We display the reductions of all 120 spectra in Figs 10 using the improved method. Here we trimmed each spectrum to show only the UV flux redward of 2300 Å, as the SNR of *Swift* spectra generally deteriorates dramatically below ∼2300 Å.

4.2 Data quality

The SNR of each spectrum depends on many factors such as the exposure time ($T_{\rm exp}$), distance to the SN, the amount of host-galaxy extinction, and phase. The sensitivity of the *Swift* UV grism peaks at ∼2800 Å. However, because of an SN Ia SED peaks near 4000 Å at maximum brightness, the SNR also increases from the UV to the optical (in terms of the effective wavelength). Here we report the SNR of each spectrum as a function of redshift, luminosity, rest-frame phase, and wavelength. The large range of $T_{\rm exp}$ (a factor of ∼10) for our sample complicates the comparison of other properties. To compensate for these differences, we also calculate the SNR scaled to that expected with a $T_{\rm exp} = 15$ ks exposure. This is achieved by multiplying the SNR by a factor of $\sqrt{15\,{\rm ks}/T_{\rm exp}}$ (assuming the noise is dominated by Poisson noise). This simple approximation ignores other factors such as the varying background for different SNe and detector noise, but it is sufficient for our purposes.

To investigate the effect of distance on the SNR, we select only the spectrum nearest to the peak brightness (within 5 d from the peak) for each SN. The result is shown in the upper panels of Fig. 7. Not surprisingly, the SNR of the spectrum shows strong correlation with the redshift, in a sense that SNe at higher redshift (thus more distant) tend to have lower SNR than those of more nearby SNe. We find that the trend generally follows the same direction as an inverse-square law (although with large dispersion), where the SN brightness is expected to be inversely proportional to the square of its luminosity distance (or the SNR is inversely proportional to the luminosity distance).

As noted above, the SNR of the spectrum also depends on the wavelength. Here we calculate the SNR in two separate regions: 2300–2800 Å (mid-UV) and 2900–4000 Å (near-UV). We find that the SNR decreases dramatically at shorter wavelengths. The SNR in the near-UV is on average ∼10 times higher than that in the mid-UV region.

We show the SNR of the (near-peak) spectrum as a function of SN *V*-band peak brightness in the middle panels of Fig. 7. Most of the SNe in our sample are brighter than $V = 15$ mag at peak, with the brightest object having $V \approx 10$ mag (SN 2011fe) and the faintest object having $V \approx 15.6$ mag (SN 2016eoa). The relation also appears to be tighter than that with redshift, and thus will be

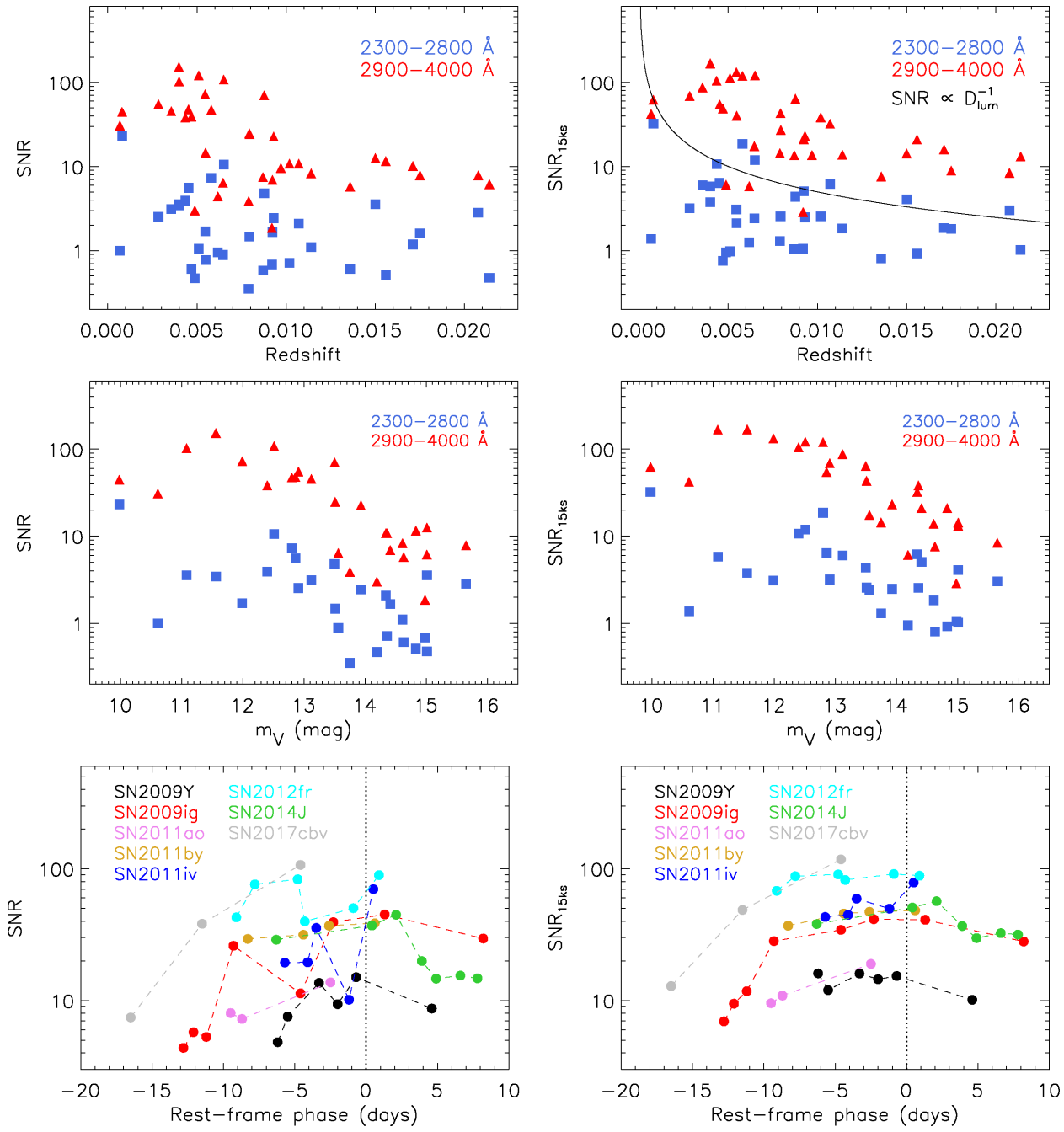

Figure 7. *Upper-left panel*: Signal-to-noise ratio (SNR) of the *Swift* sample as the function of redshift. Here we select the spectrum closest to the peak brightness (within 5 d) of each SN for comparison. The SNRs are determined for 2300–2800 Å (mid-UV) and 2900–4000 Å (near-UV) and displayed as blue squares and red triangles, respectively. *Upper-right panel*: Same as the upper-left panel, but scaling the SNR to that expected with a $T_{\rm exp} = 15$ ks exposure (see Section 4.2 for details). The inverse-square law, flux $\propto D^{-2}$ (or SNR $\propto D^{-1}$), is overplotted (the vertical position is arbitrary). Here the variable D represents the luminosity distance of the SN. *Middle-left panel*: The SNR of the *Swift* sample as a function of V-band peak brightness. As in the upper panels, the SNR is determined from the near-peak spectrum of each SN. *Middle-right panel*: Same as the upper-right panel, but with V-band peak brightness. *Lower-left panel*: The SNR of the *Swift* sample as a function of rest-frame phase. We select the SNe which have multi-epoch observations to show the temporal variation of SNR. Here the SNR is determined for the entire spectral range (2300–5000 Å). The vertical dotted line marks the epoch of peak brightness. *Lower-right panel*: Same as the lower-left panel, but scaling the SNR to that expected with a $T_{\rm exp} = 15$ ks exposure.

useful for scheduling future observations, in estimating the SNR of the spectrum given the exposure time and SN magnitude. Note that SN 2014J has $V \approx 10.6$ mag at peak, which is the second brightest object in our sample (in terms of V-band peak brightness). However, its spectrum has a low SNR ($\sim$1 in mid-UV) due to large extinction ($A_V \approx 2$ mag; e.g. Goobar et al. 2014; Amanullah et al. 2014; Foley et al. 2014) from the dust.

In the bottom panels of Fig. 7, we show the dependence of SNR on the SN phase. By examining the SNe which have multi-epoch observations in our sample, we find the trend that the SNR of pre-

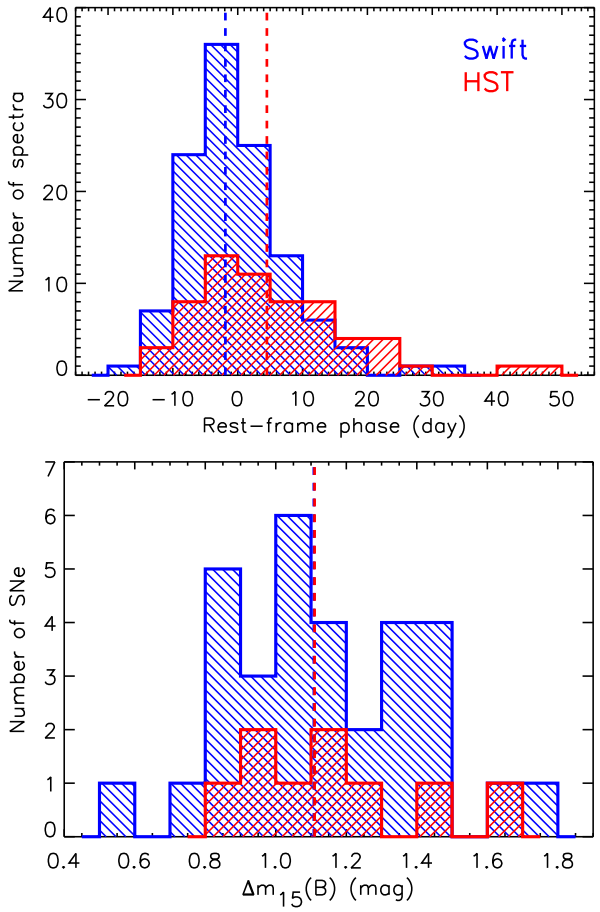

Figure 8. Phase (upper panel) and $\Delta m_{15}(B)$ (lower panel) distributions for the *Swift* sample (blue histogram) and the current *HST* UV sample (red histogram). The vertical dashed line in each panel represents the median of the distribution.

peak spectra generally rises with phase and peaks at the maximum light. It then decreases after the peak when the SN gets fainter at later phases. This trend is consistent with the SN Ia light curve, where the peak luminosity is generally 3–4 mag brighter than that right after the SN explosion (e.g. Zheng et al. 2013). The resulting variation on SNR of the spectrum can be as large as a factor of $\gtrsim$10 (assuming a fixed $T_{\rm exp}$).

4.3 Comparison to *HST* UV sample

Compared to *Swift*, the current *HST* SN Ia UV sample that probes blueward of 2900 Å is relatively small (e.g. 9 SNe in Foley et al. 2016). The addition of 39 SNe Ia observed by *Swift* greatly increases the number of SNe with UV data. Here we compare these samples.

The top panel of Fig. 8 compares the SN phase distributions of the *Swift* and Foley et al. (2016) *HST* samples. *Swift* tends to observe SNe at earlier phases than *HST*, with medians phases of −1.9 and +5.5 d, respectively. There are six *Swift*-observed SNe Ia with their first UV spectrum $\gtrsim$10 d before peak brightness. In contrast, only two *HST*-observed SNe Ia have UV observations $\gtrsim$10 d before peak brightness. As earlier observations provide critical progenitor information (e.g. Pan et al. 2015), *Swift* can be a powerful resource for studying SN Ia physics.

The bottom panel of Fig. 8 compares the $\Delta m_{15}(B)$ distributions of the *Swift* and Foley et al. (2016) *HST* samples. The *Swift* sample has a larger range of $\Delta m_{15}(B)$ and several more examples for specific values of $\Delta m_{15}(B)$. In particular, our *Swift* sample contains several slowly declining SNe Ia (e.g. $\Delta m_{15}(B) < 0.8$ mag). This will greatly increase the resolution and precision of parameter space when constructing data-driven models of SN Ia UV spectra (e.g. Foley et al. 2016).

For the subset of SNe that were observed at similar phases with both *Swift* and *HST*, we can directly compare the *Swift* data reduction to the well-calibrated *HST* data. Fig. 9 displays the 6 SNe Ia, which have high-SNR UV spectra and similar phases for both *Swift* and *HST* observations. The *Swift* spectra have been normalized to match the *HST* spectra in the region 3000–3500 Å (for SN 2017cbv, whose *HST* spectrum only covers $\lambda < 3100$ Å, we use 2500–3000 Å). We present the spectra in both linear and logarithmic scales in the figure. The spectra are generally well matched, further indicating that the *Swift* spectral reductions are accurate.

Compared to *Swift*, *HST* covers a similar wavelength range in the UV, but the *HST* spectra have consistently higher SNR.

5 SUMMARY

In this work, we present *Swift*/UVOT observations and reductions of 120 spectra of 39 nearby SNe Ia. This is the largest existing sample of SN Ia UV spectra that probe blueward of 2900 Å. The new sample doubles the number of SN Ia UV spectra and triples the number of SNe Ia with UV spectra.

We outline an improved method to reduce the *Swift* spectroscopic data and perform the reductions. This method achieves a more precise background subtraction than the original reduction pipeline. Our new method can effectively reduce the contamination from background sources, which is critical for the slitless observations of *Swift* UVOT.

Compared to the *HST* sample, the *Swift* sample is larger in both number of SNe and number of spectra. The *Swift* sample has a broad $\Delta m_{15}(B)$ distribution, spanning the entire range for SNe Ia. The *Swift* sample also has significantly more SNe at the earliest phases, with the median phase of the first observation of an SN and all spectra being −4.5 and −1.9 d, respectively.

SN Ia UV spectra are critical to understanding the progenitor systems and explosion mechanisms of SNe Ia. With the addition of *Swift* UV spectra, we are building a sample that has the statistical power to investigate the UV properties of the SN Ia sample. A detailed analysis of these data will be presented in the second paper of this series (Pan et al. in preparation).

ACKNOWLEDGEMENTS

Swift spectroscopic observations were performed under programs GI–04047, GI–5080130, GI–6090689, GI–8110089, GI–1013136, and GI–1215205; we are very grateful to N. Gehrels, S. B. Cenko, and the *Swift* team for executing the observations quickly. Based in part on observations made with the NASA/ESA *HST*, obtained at the Space Telescope Science Institute (STScI), which is operated by the Association of Universities for Research in Astronomy, Inc., under National Aeronautics and Space Administration (NASA) contract NAS 5–26555. These observations are associated with Programmes GO–12298, GO–12592, GO–13286, GO–13646, and DD–14925. This manuscript is based upon work supported by NASA under Contract No. NNG16PJ34C issued through the *WFIRST* Science Investigation Teams Programme.

We thank Steven Downing for useful discussions and comments. The referee, Peter Brown, provided suggestions that helped improve

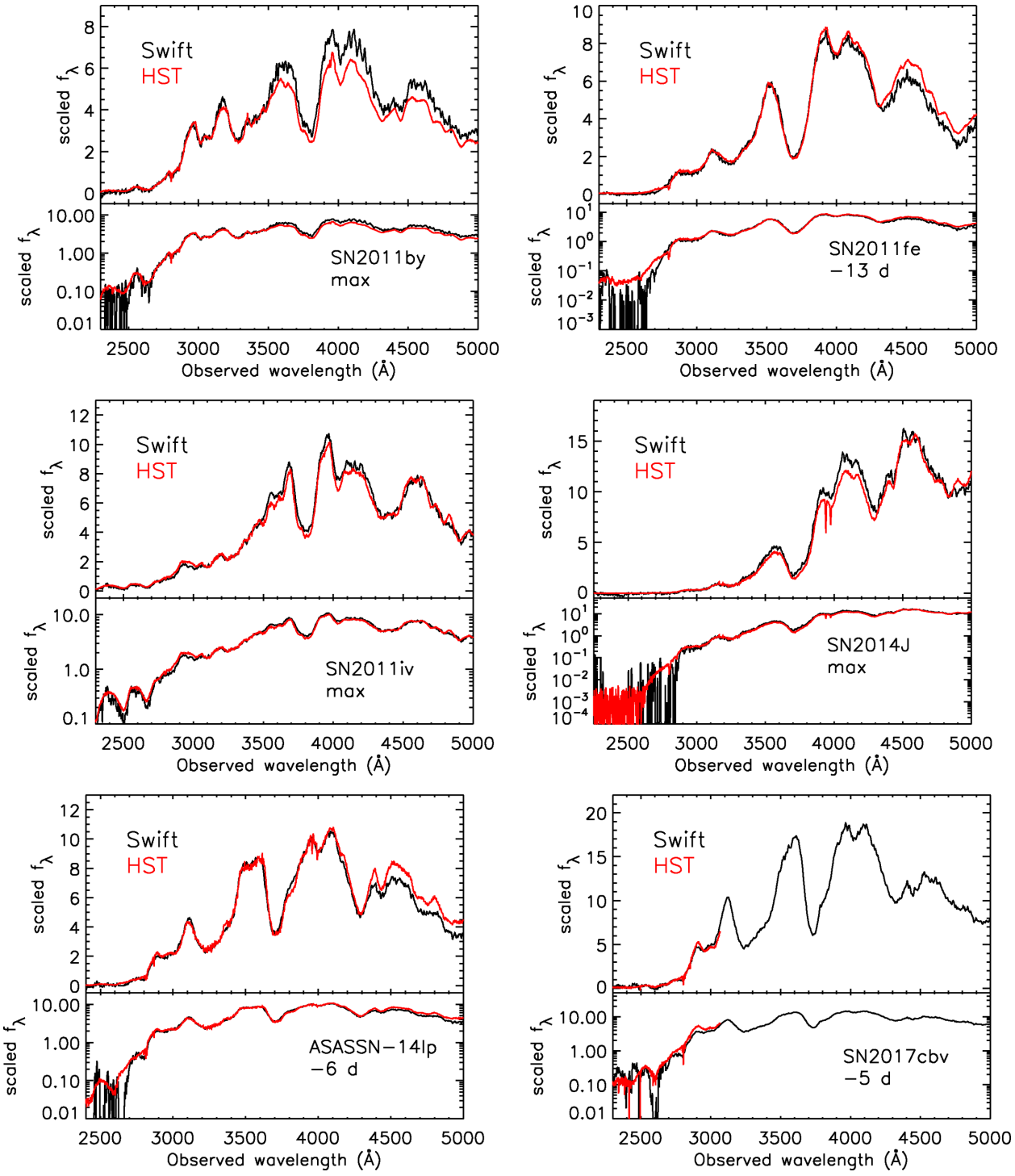

Figure 9. UV through optical spectra (2300–5000 Å) of six SNe Ia observed with both *Swift*/UVOT (black curves) and *HST*/STIS (red curves). For each SN, we display the flux with both linear (upper subpanel) and logarithmic (lower subpanel) scales. Note that for SN 2017cbv, the *HST* spectrum only covers $\lambda \lesssim 3100$ Å.

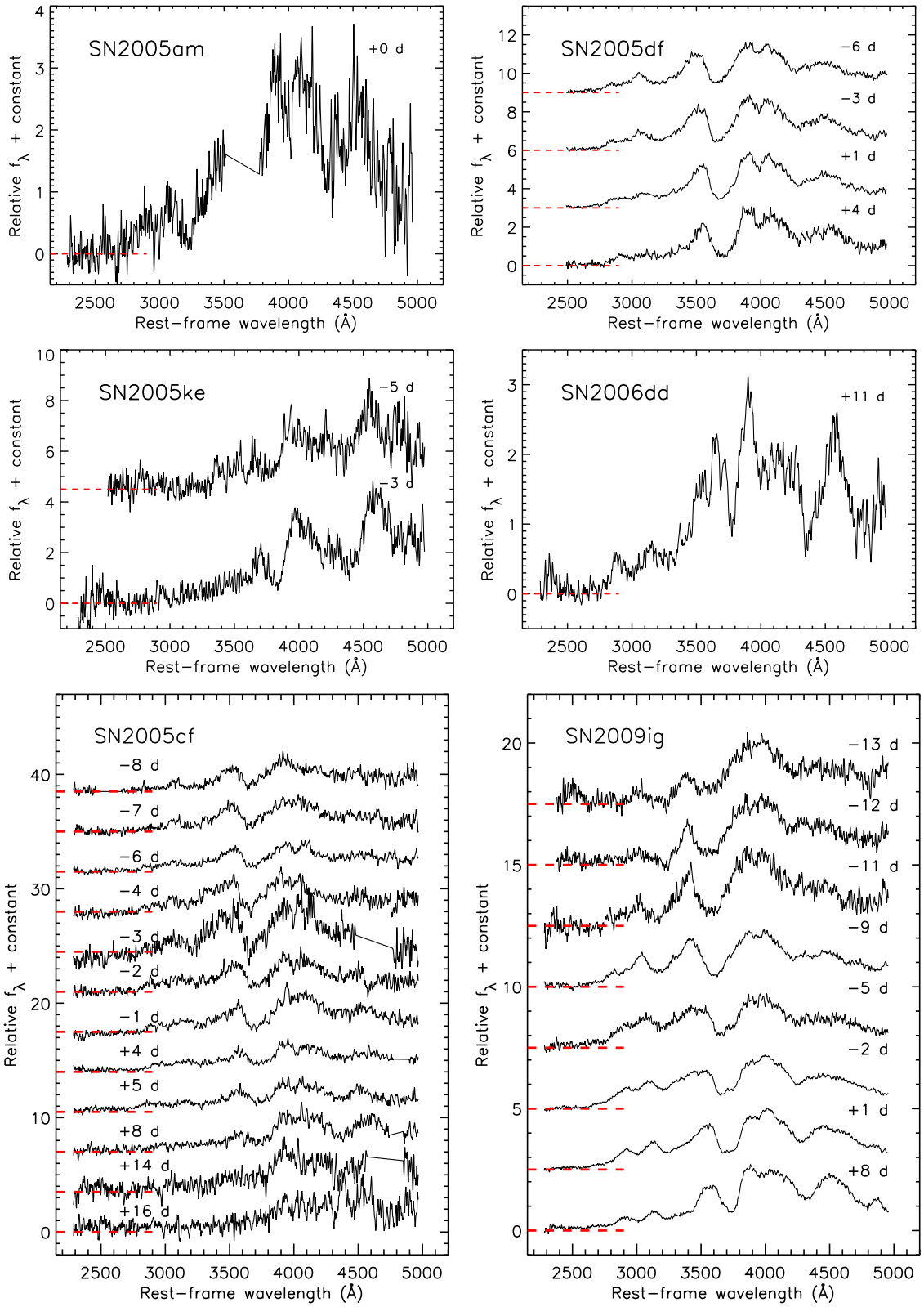

Figure 10. *Swift* UVOT grism observations of SNe Ia. The red dashed line marks the level of zero flux.

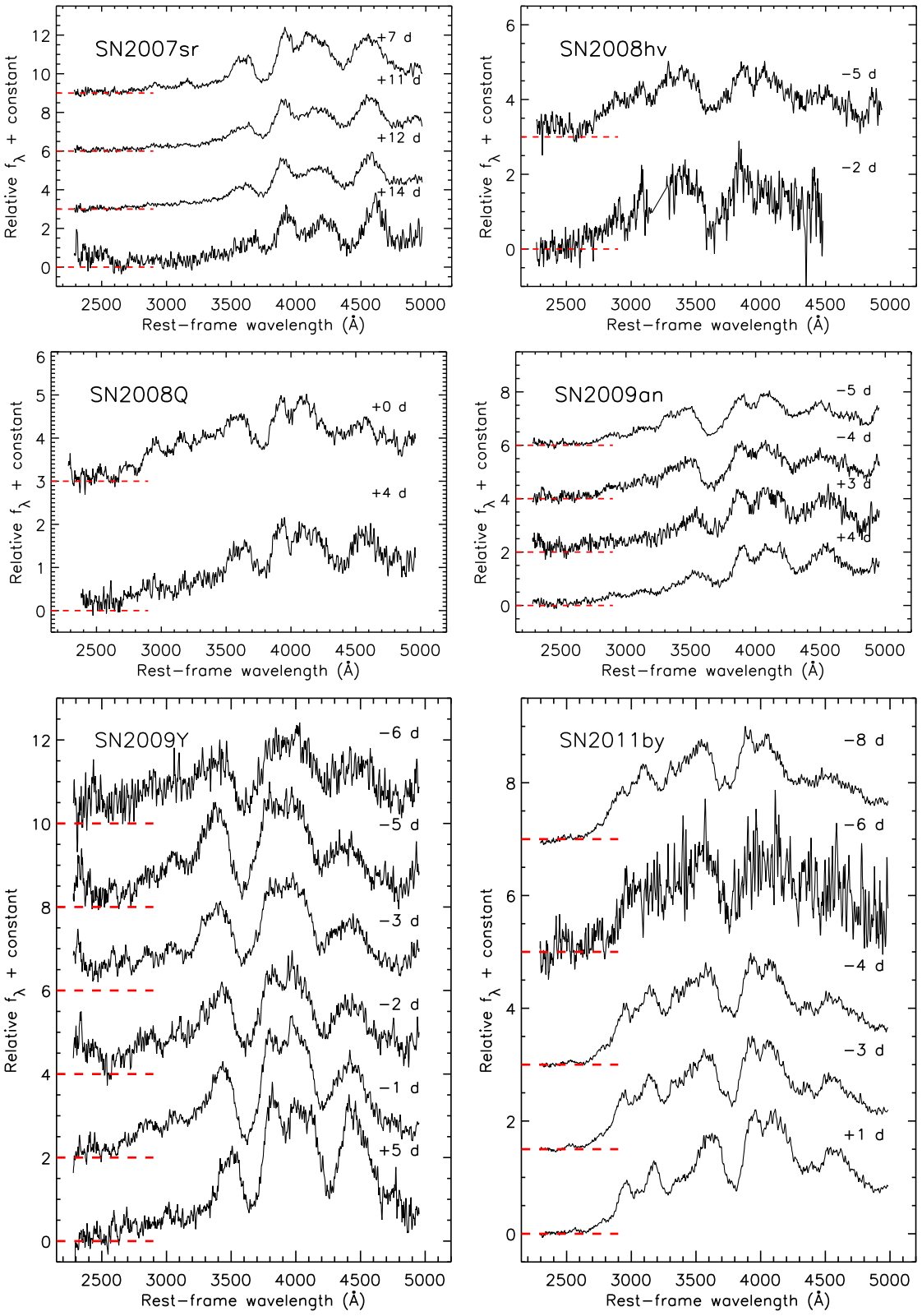

Figure 10. (continued).

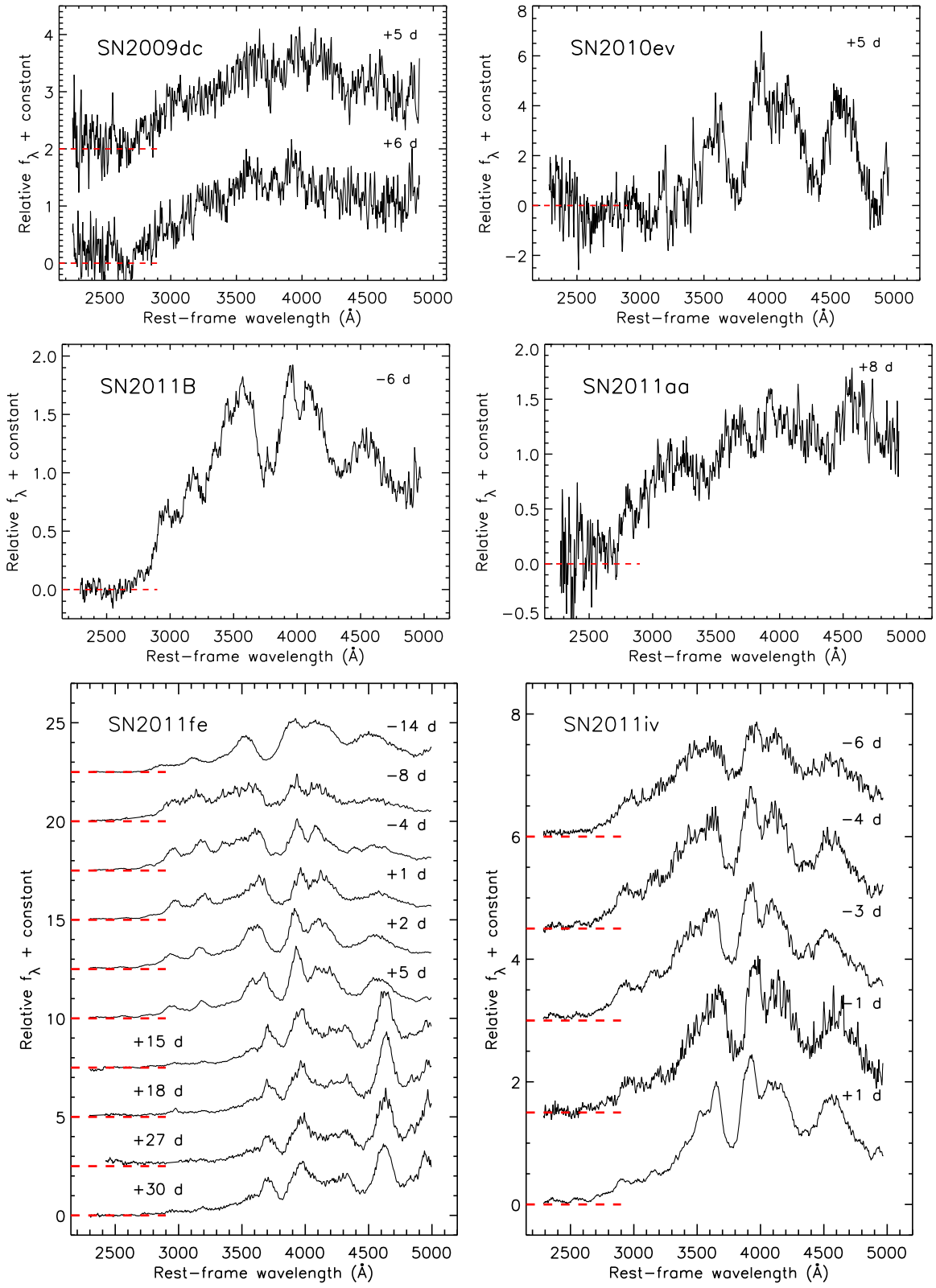

Figure 10. (continued).

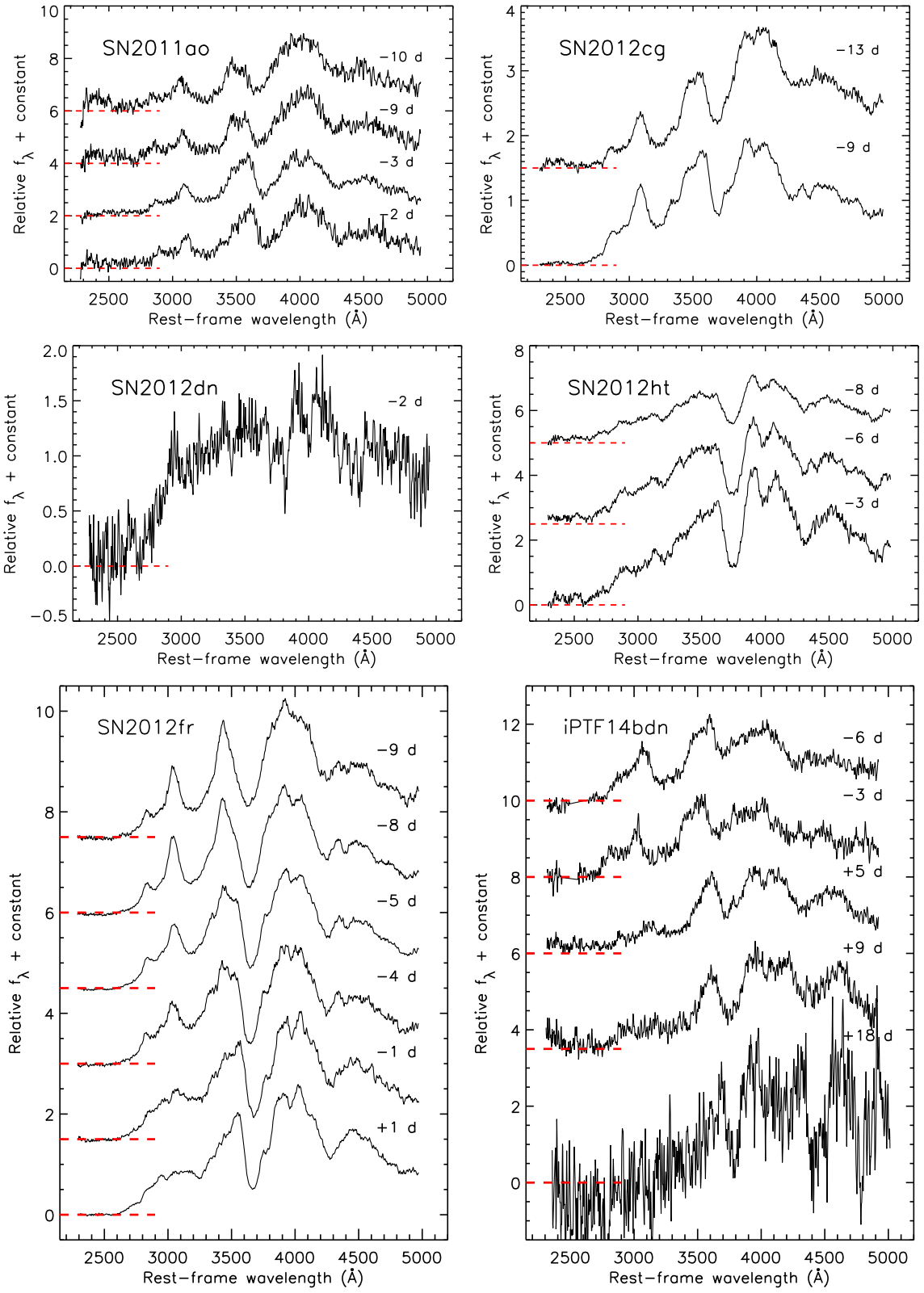

Figure 10. (continued).

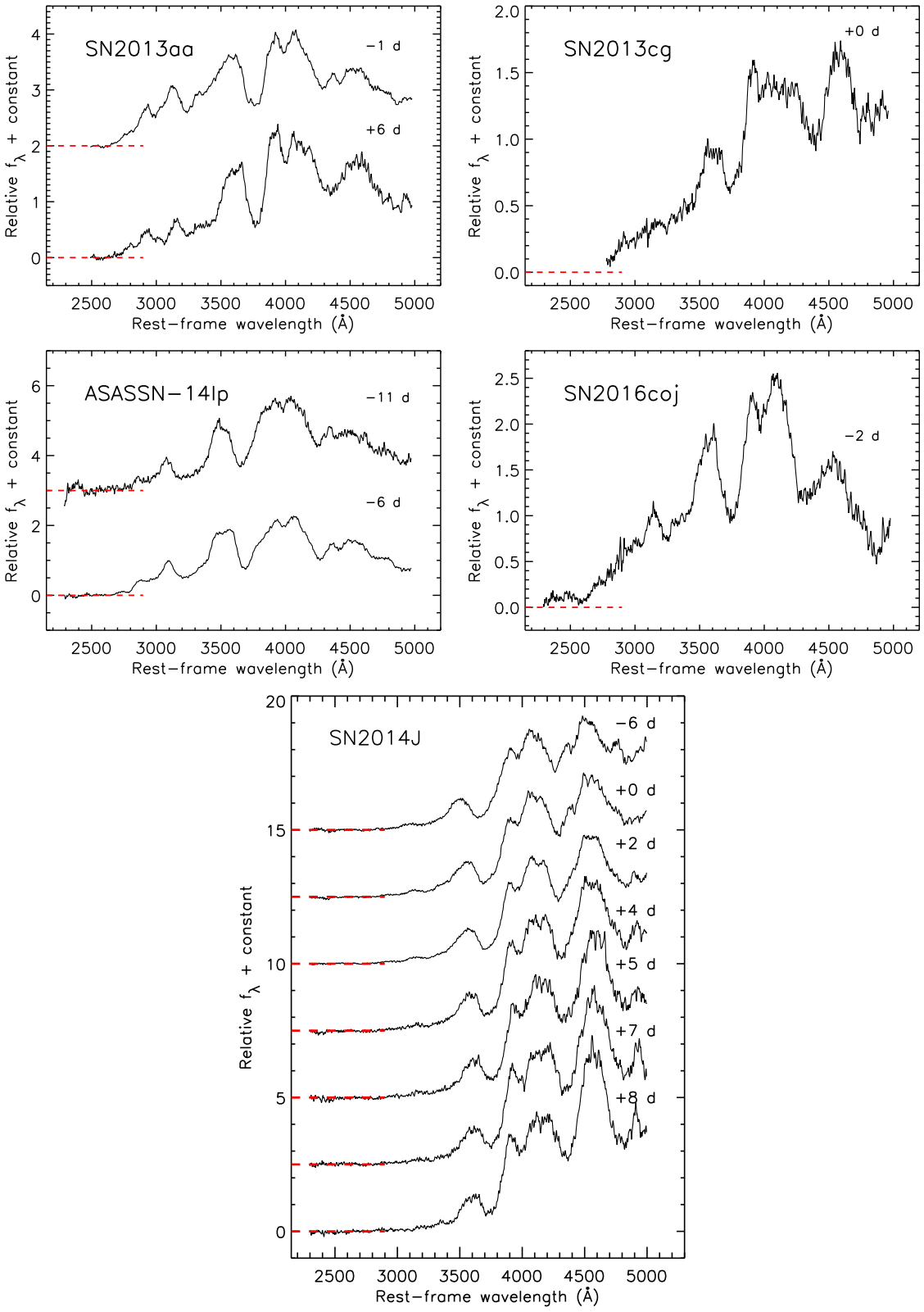

Figure 10. (continued).

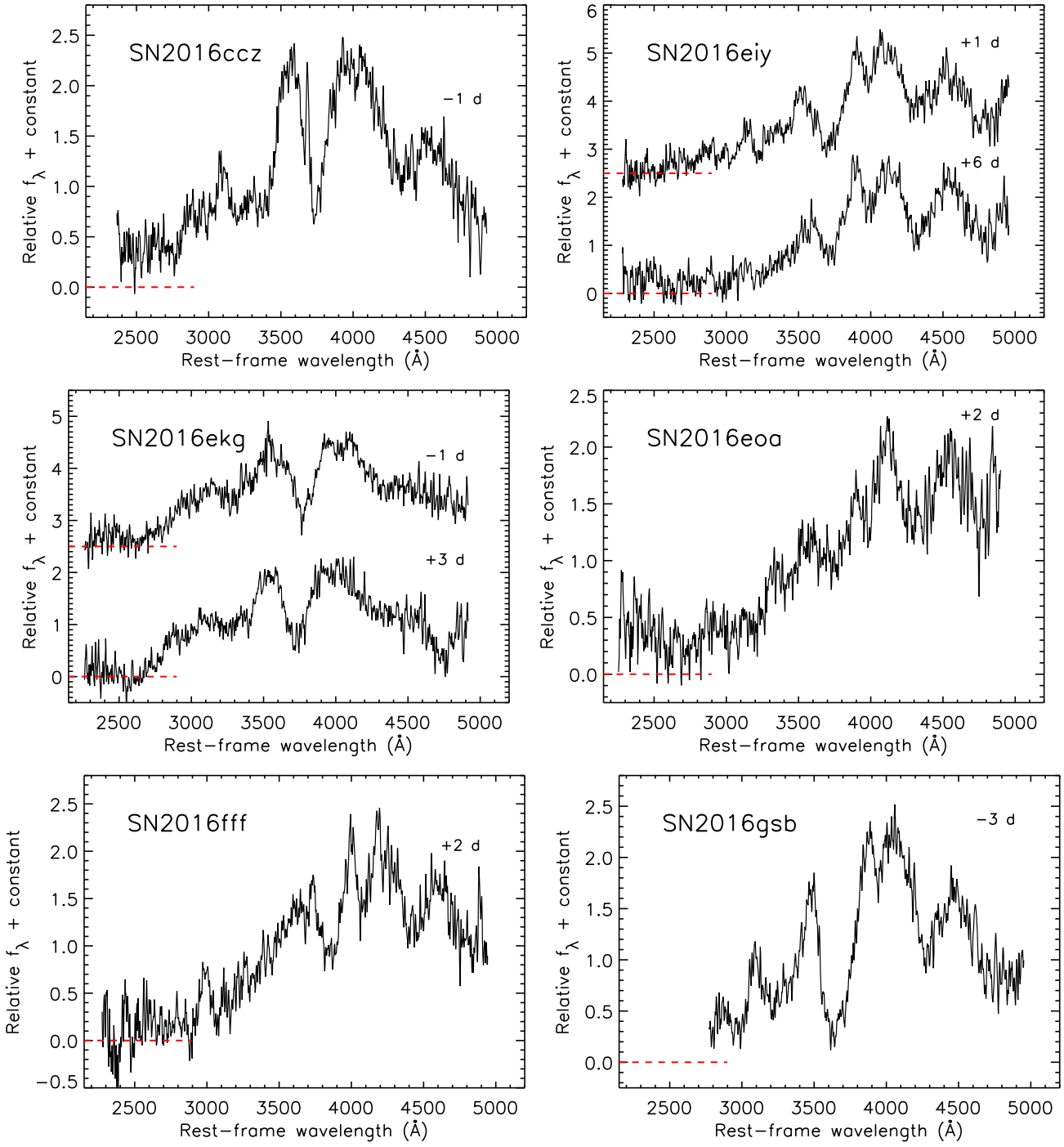

Figure 10. (continued).

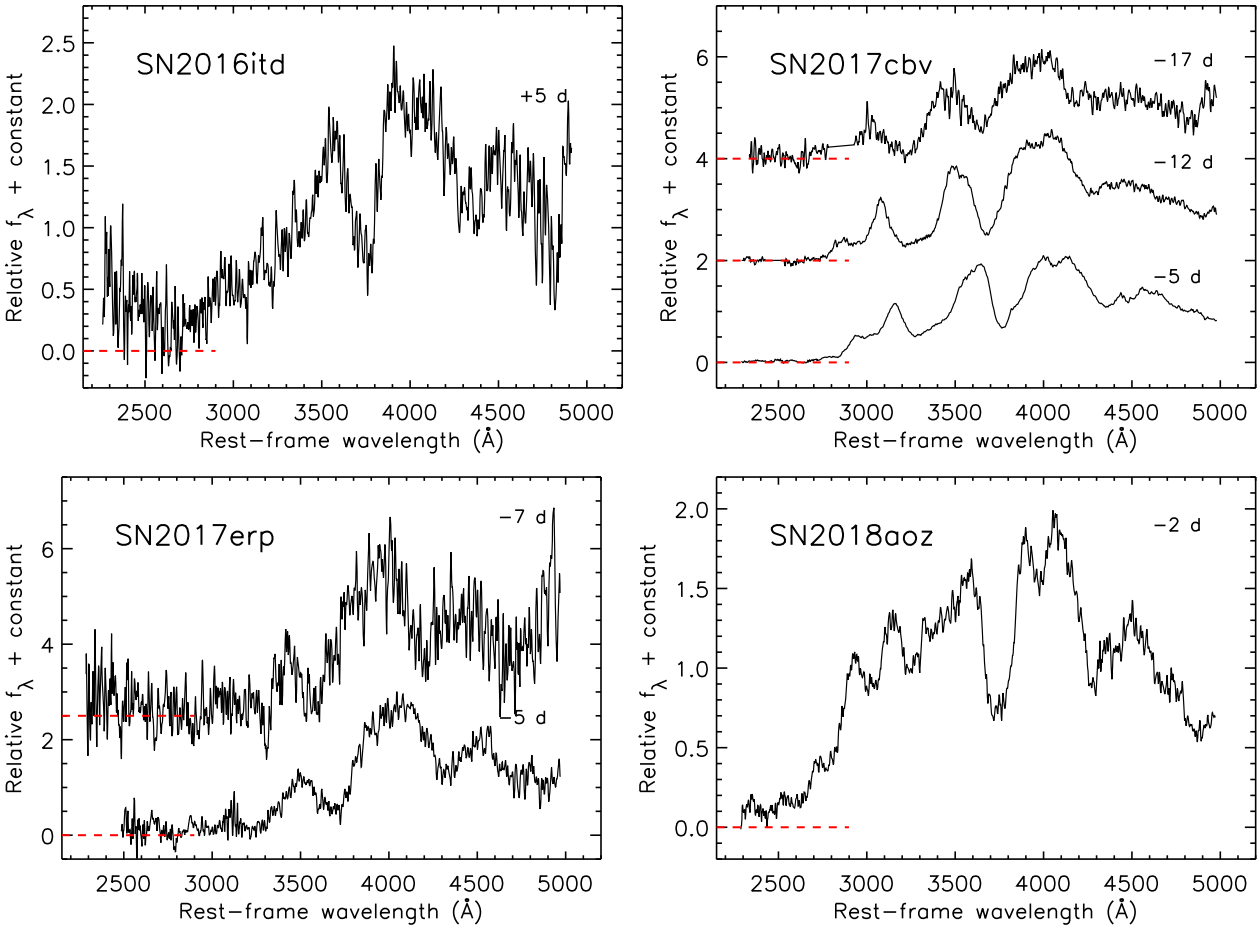

Figure 10. (continued).

this paper. NPMK has been supported by the UK Space Agency. The UCSC group is supported in part by NASA grant 14-WPS14-0048, NSF grant AST-1518052, the Gordon & Betty Moore Foundation, and by fellowships from the Alfred P. Sloan Foundation and the David and Lucile Packard Foundation to RJF. Additional financial assistance to AVF was provided by the TABASGO Foundation, the Christopher R. Redlich Fund, and the Miller Institute for Basic Research in Science (UC Berkeley).

REFERENCES

Amanullah R. et al., 2014, ApJ, 788, L21
Blondin S., Tonry J. L., 2007, ApJ, 666, 1024
Brown P. J. et al., 2005, ApJ, 635, 1192
Brown P. J. et al., 2014, ApJ, 787, 29
Brown P. J., Landez N. J., Milne P. A., Stritzinger M. D., 2017, ApJ, 836, 232
Bufano F. et al., 2009, ApJ, 700, 1456
Cappellaro E., Turatto M., Fernley J., eds, 1995, ESA SP-1189: IUE-ULDA Access Guide No. 6: Supernovae. ESA, Noordwijk
Childress M. J. et al., 2015, MNRAS, 454, 3816
Childress M. J. et al., 2016, PASA, 33, e055
Conley A. et al., 2008, ApJ, 681, 482
Folatelli G. et al., 2010, AJ, 139, 120
Folatelli G. et al., 2013, ApJ, 773, 53
Foley R. J., Kirshner R. P., 2013, ApJ, 769, L1
Foley R. J. et al., 2012a, ApJ, 744, 38
Foley R. J. et al., 2012b, ApJ, 753, L5
Foley R. J. et al., 2014, MNRAS, 443, 2887
Foley R. J. et al., 2016, MNRAS, 461, 1308
Foley R. J. et al., 2018, MNRAS, 475, 193
Friedman A. S. et al., 2015, ApJS, 220, 9
Gall C. et al., 2017, A&A, 611, A58
Gehrels N. et al., 2004, ApJ, 611, 1005
Goobar A. et al., 2014, ApJ, 784, L12
Hillebrandt W., Niemeyer J. C., 2000, ARA&A, 38, 191
Hillebrandt W., Kromer M., Röpke F. K., Ruiter A. J., 2013, Frontiers Phys., 8, 116
Hoeflich P., Khokhlov A., Wheeler J. C., Phillips M. M., Suntzeff N. B., Hamuy M., 1996, ApJ, 472, L81
Hosseinzadeh G. et al., 2017, ApJ, 845, L11
Kelly P. L., Hicken M., Burke D. L., Mandel K. S., Kirshner R. P., 2010, ApJ, 715, 743
Kelly P. L., Filippenko A. V., Burke D. L., Hicken M., Ganeshalingam M., Zheng W., 2015, Science, 347, 1459
Krisciunas K., Suntzeff N. B., Espinoza J., Gonzalez D., Miranda A., Sanhueza P., 2017, Res. Notes Am. Astron. Soc., 1, 36
Kuin P., 2014, Astrophysics Source Code Library, ascl:1410.004
Kuin N. P. M. et al., 2015, MNRAS, 449, 2514
Lampeitl H. et al., 2010, ApJ, 722, 566
Lentz E. J., Baron E., Branch D., Hauschildt P. H., Nugent P. E., 2000, ApJ, 530, 966
Maguire K. et al., 2012, MNRAS, 426, 2359
Maguire K. et al., 2013, MNRAS, 436, 222
Maoz D., Mannucci F., Nelemans G., 2014, ARA&A, 52, 107
Monet D. G. et al., 2003, AJ, 125, 984
Munari U., Henden A., Belligoli R., Castellani F., Cherini G., Righetti G. L., Vagnozzi A., 2013, New Astron., 20, 30

Pan Y.-C. et al., 2014, MNRAS, 438, 1391
Pan Y.-C. et al., 2015, MNRAS, 452, 4307
Perlmutter S. et al., 1999, ApJ, 517, 565
Phillips M. M., 1993, ApJ, 413, L105
Riess A. G., Press W. H., Kirshner R. P., 1996, ApJ, 473, 88
Riess A. G. et al., 1998, AJ, 116, 1009
Roming P. W. A. et al., 2004, in Flanagan K. A., Siegmund O. H. W., eds, Proc. SPIE Conf. Ser. Vol. 5165, X-Ray and Gamma-Ray Instrumentation for Astronomy XIII. SPIE, Bellingham, p. 262
Shappee B. J. et al., 2016, ApJ, 826, 144
Silverman J. M., Ganeshalingam M., Li W., Filippenko A. V., Miller A. A., Poznanski D., 2011, MNRAS, 410, 585
Silverman J. M., Ganeshalingam M., Filippenko A. V., 2013, MNRAS, 430, 1030
Smartt S. J. et al., 2015, A&A, 579, A40
Smitka M. T., Brown P. J., Suntzeff N. B., Zhang J., Zhai Q., Wang X., Mo J., Zhang T., 2015, ApJ, 813, 30
Smitka M. T., Brown P. J., Kuin P., Suntzeff N. B., 2016, PASP, 128, 034501
Stritzinger M. et al., 2010, AJ, 140, 2036
Sullivan M. et al., 2010, MNRAS, 406, 782
Timmes F. X., Brown E. F., Truran J. W., 2003, ApJ, 590, L83
Wang X. et al., 2009a, ApJ, 697, 380
Wang X. et al., 2009b, ApJ, 699, L139
Yamanaka M. et al., 2014, ApJ, 782, L35
Zhang J.-J., Wang X.-F., Bai J.-M., Zhang T.-M., Wang B., Liu Z.-W., Zhao X.-L., Chen J.-C., 2014, AJ, 148, 1
Zheng W. et al., 2013, ApJ, 778, L15

This paper has been typeset from a TEX/LATEX file prepared by the author.